

SUZAKU OBSERVATION OF THE BRIGHTEST BROAD-LINE RADIO GALAXY 4C 50.55 (IGR J 21247+5058)

FUMIE TAZAKI¹, YOSHIHIRO UEDA¹, YUKIKO ISHINO¹, SATOSHI EGUCHI¹, NAOKI ISOBE¹,
 YUICHI TERASHIMA², RICHARD F. MUSHOTZKY³

Draft version August 5, 2010

ABSTRACT

We report the results from a deep *Suzaku* observation of 4C 50.55 (IGR J 21247+5058), the brightest broad-line radio galaxy in the hard X-ray (> 10 keV) sky. The simultaneous broad band spectra over 1–60 keV can be represented by a cut-off power law with two layers of absorption and a significant reflection component from cold matter with a solid angle of $\Omega/2\pi \approx 0.2$. A rapid flux rise by $\sim 20\%$ over 2×10^4 sec is detected in the 2–10 keV band. The spectral energy distribution suggests that there is little contribution to the total X-ray emission from jets. Applying a thermal Comptonization model, we find that corona is optically thick ($\tau_e \approx 3$) and has a relatively low temperature ($kT_e \approx 30$ keV). The narrow iron-K emission line is consistent with a picture where the standard disk is truncated and/or its inner part is covered by optically thick Comptonizing corona smearing out relativistic broad line features. The inferred disk structure may be a common feature of accretion flows onto black holes that produce powerful jets.

Subject headings: galaxies: active – galaxies: individual (4C 50.55) – X-rays: galaxies

1. INTRODUCTION

Radio galaxies are a class of Active Galactic Nuclei (AGNs) spouting powerful radio jets whose axis is not aligned along the line of sight. While the formation mechanism of relativistic jets is not fully understood, it must be closely related to mass accretion flow onto the central supermassive black hole. In fact, studies of Galactic black holes have revealed that the relative power of the jets to accretion critically depends on the state of the accretion disk, which is predominantly determined by the mass accretion rate (e.g., see Fender et al. 2004b). For AGNs, however, detailed studies of accretion disk state in relation to the jet formation are still limited. Broad band observation of nearby, bright radio galaxies hence give us ideal opportunities to unveil this problem, because, unlike “blazars”, the innermost disk can be well observable in the X-ray band with much smaller contribution from the jet emission.

4C 50.55 (IGR J21247+5058) is a Fanaroff-Riley type II broad line radio galaxy (BLRG), discovered by *INTEGRAL* in its first survey catalogue (Bird, Barlow & Bassani 2004). The source is also detected in the first 9 months data of *Swift* Burst Alert Telescope (BAT) survey of AGNs (Tueller et al. 2008). Though being the brightest BLRG in the hard X-ray sky above 10 keV, 4C 50.55, located at $(l, b) = (93.32, 0.3937)$, had been unrecognized as a bright X-ray source until the *INTEGRAL* and *Swift* era, due to the obscuration by the Galactic plane. This source is also of great interest for understanding the accretion flow onto supermassive black holes at high fractions of Eddington luminosity, which is estimated to be $L_{\text{bol}}/L_{\text{Edd}} \sim 0.4$ (see section 3.5). Massetti et al. (2004) determined the red-

shift to be $z = 0.020 \pm 0.001$ based on the detection of a broad H α emission line in the optical spectrum. From the observed flux densities at 1.4 GHz with the Very Large Array (VLA), Molina et al. (2007) estimate the inclination angle to be $\theta \sim 35^\circ$, assuming a Lorentz factor of $\gamma = 5$ and a typical power ratio between the core and total known for radio galaxies (Giovannini et al. 1988). The inferred viewing geometry of the nucleus is well consistent with the classification of 4C 50.55 as a BLRG.

The initial results on the X-ray spectra are reported by Molina et al. (2007), who used the *XMM-Newton* and *Swift*/XRT data combined with a time-averaged *INTEGRAL* spectrum. They find that the spectra below 10 keV are apparently hard, and complex, multiple layers of absorber are required. Iron-K features are not significantly detected and the strength of reflection components, $R \equiv \Omega/2\pi$, where Ω is the solid angle of the reflector, is not tightly constrained ($R \lesssim 0.9$). In this paper, we present the first simultaneous broad band X-ray data of 4C 50.55 observed with *Suzaku* (Mitsuda et al. 2007), obtained in a different epoch of the *XMM-Newton* observation. *Suzaku* carries (then available) three CCD cameras called the X-ray Imaging Spectrometers, XIS-0, XIS-3 (Front-side Illuminated XIS; XIS-FI), and XIS-1 (Back-side Illuminated XIS; XIS-BI), and a collimated-type instrument called the hard X-ray detector (HXD), which consists of Si PIN photo-diodes and GSO scintillation counters. The XISs and HXD-PIN covers the 0.2–12 keV and 10–70 keV, respectively. Since AGNs are time variable, the simultaneous coverage is critical for studying the continuum shape over the broad band, in particular to accurately constrain the Compton reflection component. Moreover, the *Suzaku* exposure is quite deep (a net exposure of ~ 100 ksec), and thus provides us with the best quality dataset so far obtained from this source.

The organization of our paper is as follows. First, we describe our *Suzaku* observation and data reduction in section 2. Next, we present the analysis and results in

¹ Department of Astronomy, Kyoto University, Kyoto 606-8502, Japan

² Department of Physics, Ehime University, Matsuyama 790-8577, Japan

³ Department of Astronomy, University of Maryland, College Park, MD, USA

section 3. The results of the *Swift*/BAT data are also presented, whose spectrum averaged over 22 months is utilized to constrain the highest energy band up to 200 keV. We plot the spectral energy distribution of 4C 50.55 from the radio to Gamma-ray bands to discuss the possible contribution of the jet component. Finally, we discuss our results in comparison with the previous studies of this target and other radio galaxies in section 4. In all spectral analysis, we apply the Galactic absorption fixed at $N_{\text{H}}^{\text{gal}} = 1.0 \times 10^{22} \text{ cm}^{-2}$ (Kalberla et al. 2005). The cosmological parameters (H_0 , Ω_{m} , Ω_{λ}) = (71 km s $^{-1}$ Mpc $^{-1}$, 0.27, 0.73; Komatsu et al. 2009) are adopted in calculating the luminosities. The errors attached to spectral parameters correspond to those at 90% confidence limits.

2. OBSERVATIONS AND DATA REDUCTION

4C 50.55 was observed with *Suzaku* from 2007 April 16 14:05 (UT) to April 18 11:04 (UT) (observation ID 702027010), focused on the nominal center position of the Hard X-ray Detector (HXD). The net exposures after data screening, described below, are 85.0 ksec (XIS-0, 1), 80.0 ksec (XIS-3), 54.7 ksec (PIN). For the HXD, we use only data collected with the PIN diodes, because we find that the signal from the source in the GSO data is not significant over the systematic error of $\approx 2\%$ in the non X-ray background (NXB) (Fukazawa et al. 2008). We use FTOOLS (heasoft version 6.6.2) to extract data, and XSPEC version 11.3.2ag for spectral fitting.

2.1. XIS Data Reduction

To apply the latest calibration, we reprocess the unfiltered event files of the XIS data according to the procedures written in *The Suzaku Data Reduction Guide (ABC Guide)*. We select the data where the time since the South Atlantic Anomaly (T.SAA) passage is longer than 436 sec, the elevation angle (ELV) is larger than 5° , and the dye-elevation angle (DYE-ELV) is larger than 20° . The XIS events are extracted from a circular region centered on the source peak, and the background is taken from a source-free region with the same distance from the optical axis as the target. We generate RMF files with *xisrmfgen*, and ARF files with *xissimarfgen* (Ishisaki et al. 2007). We examine the spectra of the ^{55}Fe calibration source (producing an Mn K α line at 5.895 keV) located on the corners of the XIS chips to check the accuracy of the energy response. By fitting them with Gaussians, we are able to reproduce the right central energy within the statistical errors and line widths of 3.9 (< 19.2) eV (XIS-0), 0.0 (< 15.6) eV (XIS-1), and 0.0 (< 14.0) eV (XIS-3). This verifies that both energy scale and energy resolution in the responses are well reliable.

2.2. HXD-PIN Data Reduction

We also reprocess the unfiltered event files of the HXD data as well. This includes the time assignment (with *hxdtime*), gain correction (*hxdpi*), and grade classification (*hxdgrade*). We select data where the time after the SAA passage is longer than 500 sec, a cutoff rigidity (COR) is larger than 6 GV, and the elevation from the earth is larger than 5° . We utilize the “tuned” NXB event files provided by the HXD team to produce the

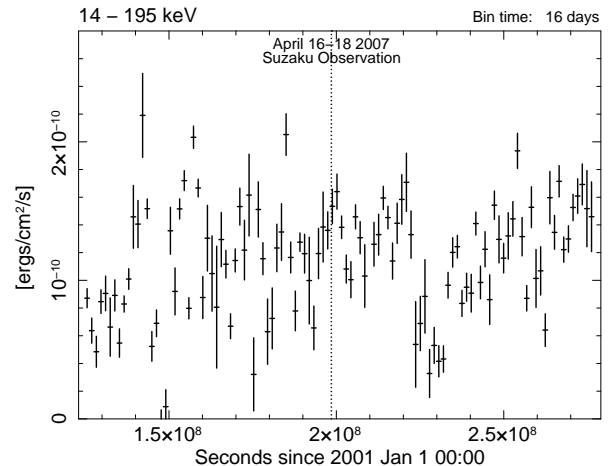


FIG. 1.— Long term light curve of 4C 50.55 in the 14–195 keV band obtained with *Swift*/BAT with 16 days bin. The fluxes are converted from the count rate by assuming a power law photon index of $\Gamma = 1.7$. The dotted lines indicate the period of the *Suzaku* observation (from 2007 April 16 to April 18).

background spectra, to which the cosmic X-ray background (CXB) based on the formula by Gruber et al. (1999) is added. We use the HXD/PIN response file *ae_hxd_pinhxname3_20080129.rsp*.

3. ANALYSIS AND RESULTS

3.1. *Swift*/BAT Data

Figure 1 shows the long term light curve of 4C 50.55 in the 14–195 keV band obtained with *Swift*/BAT from 2004 December 15 to 2009 October 10. Each data point corresponds to the averaged flux for 16 days. Time variability is clearly noticed. The epoch of our *Suzaku* observation is indicated by the dashed line in the figure. The time-averaged BAT spectrum over the first 22 months covering the 14–195 keV band is plotted in Figure 2. We find that it can be fit with a single power law of $\Gamma = 1.68 \pm 0.25$. The time averaged 14–195 keV flux is $1.7 \times 10^{-10} \text{ ergs cm}^{-2} \text{ s}^{-1}$ (based on the best-fit power law model), which corresponds to a luminosity of $1.5 \times 10^{44} \text{ ergs s}^{-1}$ in the rest-frame 14.3–199 keV band. In the subsequent subsections, we will apply more realistic spectral models to this spectrum.

3.2. *Suzaku* Light Curve

We make the *Suzaku* light curves of 4C 50.55 with a 5760 sec bin, the orbital period of the satellite, to remove any possible modulation related to the orbital condition. Figure 3 shows the X-ray light curves obtained with the XIS-FIs (2–10 keV, *upper*) and with the HXD/PIN (15–40 keV, *middle*), and their hardness ratio (PIN/XIS, *lower*). The zero point of time corresponds to the start time of the *Suzaku* observation. The XIS light curve in the 2–10 keV band indicates a rapid flux increase by $\sim 20\%$ in the last 20 ksec exposure. The time scale of this variability is $\sim 10^4 \text{ sec}$, indicating that the emission region is within $\sim 30r_g$ ($r_g \equiv \frac{GM}{c^2}$ is the gravitational radius) for a black hole mass of $M = 10^{7.8} M_\odot$ (see section 3.5). By contrast, the light curve in the 15–40 keV band does not show evidence for significant variability above the statistical errors in the same epoch. Thus,

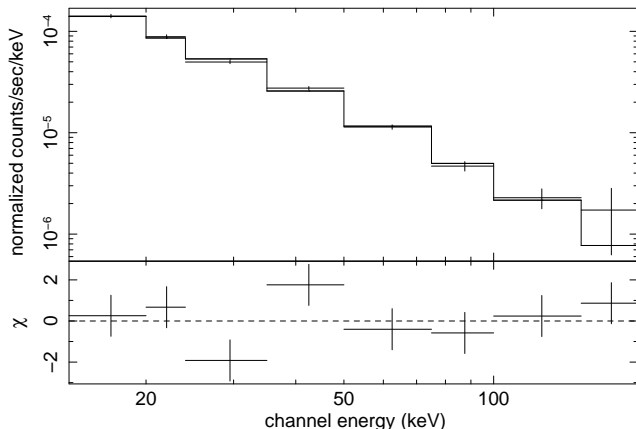


FIG. 2.— The time-averaged *Swift*/BAT spectrum of 4C 50.55 over 22 months. The best-fit model is a pexriv model (see Table 1).

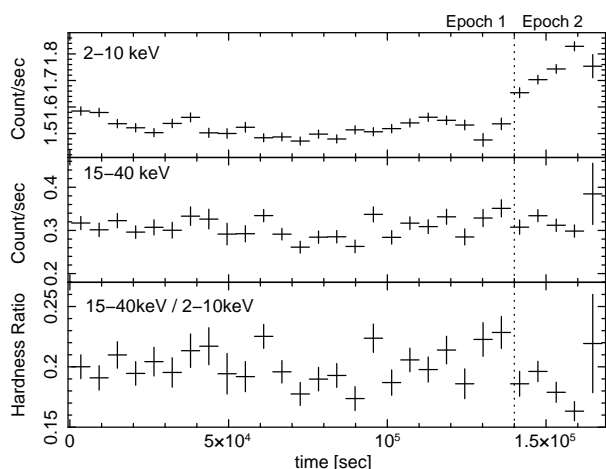


FIG. 3.— Light curves of 4C 50.55 obtained by the *Suzaku* observation, with a 5760 sec bin. The start time corresponds to 2007 April 16. The dotted line shows the border between epochs 1 and 2. (*upper*) the light curve of XIS-FIs in the 2–10 keV band. (*middle*) that of PIN in the 15–40 keV band. (*lower*) the hardness ratio between them (15–40 keV / 2–10 keV).

there is a hint for decrease in the hardness ratio between the PIN and XIS, although its significance is marginal. For the following spectral analysis, we separate the observation period into two, epoch 1 ($0\text{--}1.4 \times 10^5$ sec) and epoch 2 ($1.4 \times 10^5\text{--}1.7 \times 10^5$ sec).

3.3. Spectral Analysis with Phenomenological Models

3.3.1. Individual Fit to the *Suzaku* and *Swift* Data

We analyze the *Suzaku* spectra of epoch 1 and epoch 2 separately, by performing simultaneous fit to those of the XIS-FIs in the 1–9 keV band, the XIS-BI in the 1–8 keV band, and the HXD/PIN in the 12–60 keV band. Given the fact that the spectrum of 4C 50.55 is subject to a heavy Galactic absorption, we do not utilize the XIS-BI data below 1 keV to avoid any possible uncertainties in the response. We find that the effects of pile-up are significant above 9.0 keV for the XIS data. Further, we discard the XIS data of the 1.7–1.9 keV band because of calibration uncertainties associated with the instrumen-

tal Si-K edge. In the simultaneous fit, the flux normalizations for the XIS-FIs and XIS-BI are set free, while that of the PIN is fixed at 1.18 relative to that of the XIS-FIs (Maeda et al. 2008).

We firstly apply a single power law model (modified by the Galactic absorption fixed at $N_{\text{H}}^{\text{gal}} = 1.0 \times 10^{22} \text{ cm}^{-2}$) to the XIS and PIN data in epoch 1, covering the 1–60 keV band. The fit is found to be far from acceptable ($\chi^2/\text{dof} = 13035/810$) and results in a very flat slope, $\Gamma \approx 1.2$. This is because the spectral shape below 10 keV is much harder than that above 10 keV. Next we apply a cut-off power law model, in the form of $E^{-\Gamma} \times \exp(-E/E_{\text{cut}})$, over which a narrow Gaussian is added to represent an iron-K emission line at 6.4 keV. We obtain $\Gamma \approx 0.83$ and $E_{\text{cut}} \approx 14$ keV with $\chi^2/\text{dof} = 4616/808$. There remain strong absorption features around 1 keV suggesting intrinsic absorption, however. When we add another absorption at the source redshift ($z = 0.02$), the fit becomes much better, yielding $\Gamma = 1.39 \pm 0.02$, $E_{\text{cut}} = 45 \pm 2$ keV, and $N_{\text{H}} = (0.67 \pm 0.01) \times 10^{22} \text{ cm}^{-2}$ with $\chi^2/\text{dof} = 997/807$. Finally, similar to the analysis done by Molina et al. (2007), we consider double absorber model with two different column densities, N_{H}^1 and N_{H}^2 , whose covering fraction is f and $(1-f)$, respectively. The fit is significantly improved ($\chi^2/\text{dof} = 940/805$) with $\Gamma = 1.61^{+0.03}_{-0.05}$, $E_{\text{cut}} = 140^{+46}_{-20}$ keV, $N_{\text{H}}^1 \approx 8.3 \times 10^{22} \text{ cm}^{-2}$, $N_{\text{H}}^2 \approx 0.73 \times 10^{22} \text{ cm}^{-2}$, and $f = 0.19$. The photon index becomes a reasonable value for AGNs. Note that our “double absorber” model has three free parameters for the absorber, while the “double partial covering” model (“**pcf*pcf***” in the XSPEC terminology) adopted by Molina et al. (2007) has four. Since the latter model does not give a significant improvement for our data ($\Delta\chi^2 \approx 1$), we adopt the former as a base continuum model for the following analysis.

The high quality *Suzaku* spectra are quite useful to constrain the reflection component, which is indicated by the presence of the iron-K emission line. Thus, we include it by utilizing our modified version of “pexriv” reflection code (Magdziarz & Zdziarski 1995) that assumes a cutoff power law continuum and contains a self-consistent fluorescence iron-K line calculated according to the same algorithm as described in Zycki et al. (1999). The additional free parameter is the relative reflection strength, $R(\equiv \Omega/2\pi)$, while we fix the ionization parameter, temperature, and inclination angle at 0, 10^5 K, and 35 degrees (Molina et al. 2007), respectively. The solar Fe abundance by Anders & Grevesse (1989) ($\text{Fe}/\text{H} = 4.68 \times 10^{-5}$) is assumed. Considering that the reflection most likely occurs in the accretion disk, we smear both reflected continuum and iron-K emission line by the “**diskline**” kernel (Fabian et al. 1989). The innermost radius r_{in} is set as a free parameter by assuming an emissivity law of r^{-3} for a fixed outer radius $r_{\text{out}} = 10^5 r_{\text{g}}$. When constraining r_{in} , we utilize only the XIS spectra around the iron-K band (3–9 keV for the XIS-FIs and 3–8 keV for the XIS-BI) and fix all the other parameters except for the normalization. Thus, the spectral fit is performed by iteration; after r_{in} is determined from the XIS-only fit, it is then fixed when finally determining the continuum parameters in the XIS+PIN fit.

The results of the spectral fit to the individual *Suzaku* spectra in epochs 1 and 2 are summarized in Table 1.

TABLE 1
BEST-FIT PARAMETERS OF CUT-OFF POWER LAW MODEL TO
THE INDIVIDUAL *Suzaku* AND *Swift* DATA

| Parameters | Epoch 1 | Epoch 2 | <i>Swift</i> /BAT |
|---------------------------------|------------------------------|-----------------------|------------------------|
| (a) f_{2-10} keV | 7.4×10^{-11} | 8.5×10^{-11} | — |
| (a) f_{10-60} keV | 1.6×10^{-10} | 1.6×10^{-10} | — |
| (a) f_{14-195} keV | — | — | 1.7×10^{-10} |
| (b) $N_{\text{H}}^{\text{gal}}$ | 1.0^{\S} | 1.0^{\S} | — |
| Γ | 1.61 ± 0.05 | 1.64 ± 0.03 | $1.68^{+0.23}_{-0.25}$ |
| E_{cut} [keV] | 80^{+36}_{-19} | 68^{+29}_{-16} | 127^{+340}_{-57} |
| $R(= \Omega/2\pi)$ | 0.18 ± 0.04 | * | 0.18^{\S} |
| (c) f | $0.19^{+0.03}_{-0.04}$ | 0.19^{\S} | — |
| (d) N_{H}^1 | $7.6^{+1.5}_{-1.4}$ | 7.6^{\S} | — |
| (d) N_{H}^2 | 0.73 ± 0.03 | 0.73^{\S} | — |
| EW [eV] | 22 | 19 | — |
| $r_{\text{in}}[r_{\text{g}}]$ | $720^{\S} (> 340)^{\dagger}$ | 720^{\S} | 720^{\S} |
| χ^2/dof | 916.0/805 | 190.8/175 | 8.594/5 |

NOTE. — Errors are 90% confidence level for a single parameter.

(a) Observed fluxes in the 2–10 keV, 10–60 keV, and 14–195 keV bands, in units of $\text{ergs cm}^{-2} \text{s}^{-1}$.

(b) Galactic absorption column density in units of 10^{22} cm^{-2} .

(c) Covering fraction

(d) Intrinsic absorption column density at the source redshift in units of 10^{22} cm^{-2} .

\S Parameters fixed at these values.

* We assume the same reflection component as that determined in epoch 1.

\dagger We constrain the inner radius only from the 3–9 keV XIS spectra in epoch 1, which is then fixed at the best-fit when determining the continuum parameters.

Figure 4 shows the XIS+PIN spectra folded by the energy responses, over which the best-fit models are plotted, with residuals in the lower panel. The expanded figure of the XIS spectra between 3–9 keV in epoch 1 is plotted in Figure 5. To emphasize the iron-K line feature, the residuals when the line is excluded from the model are shown in the lower panel of this figure. From epoch 1, we obtain $\Gamma = 1.61 \pm 0.05$, $E_{\text{cut}} = 80^{+36}_{-19}$ keV, and $R = 0.18 \pm 0.04$. The innermost radius is constrained to be $r_{\text{in}} = 720r_{\text{g}} (> 340r_{\text{g}})$ from the XIS data. For the analysis of the epoch 2 spectra, we assume the same parameters of the reflection component (including its absolute flux) as those found from the epoch 1 data, since it is very unlikely that it varied on such a short time scale of $< 10^4$ sec. The parameters of the absorption are fixed to the epoch 1 values as well. Thus, only free parameters are Γ , E_{cut} , and the normalization. Finally, we also perform spectral fit to the time-averaged *Swift*/BAT spectrum by adopting the same model. The reflection strength is fixed at $R = 0.18$ referring to the epoch 1 result. The best-fit model is over-plotted in Figure 2, whose parameters are summarized in Table 1.

3.3.2. Simultaneous Fit to the *Suzaku* and *Swift* Data

From the above analysis, we find no significant differences in the spectral parameters (except for the normalization) within the statistical errors between the *Suzaku* epoch 1, epoch 2, and *Swift*/BAT data, although there is a hint that the spectrum became slightly softer in epoch 2. Thus, to best constrain the continuum parameters, in particular the cutoff energy, we study the *Suzaku*

TABLE 2
BEST-FIT PARAMETERS OF CUT-OFF POWER LAW MODEL TO THE
COMBINED *Suzaku* AND *Swift* DATA

| Parameters | Epoch 1 | Epoch 2 (1) | Epoch 2 (2) |
|---------------------------------|---------------------|-------------------|------------------------|
| (a) L_{2-10} keV | 8.1 | 9.3 | 9.0 |
| (b) $N_{\text{H}}^{\text{gal}}$ | 1.0^{\S} | 1.0^{\S} | 1.0^{\S} |
| Γ | 1.65 ± 0.04 | 1.69 ± 0.02 | 1.65^{\S} |
| E_{cut} [keV] | 105^{+28}_{-19} | 127^{+25}_{-23} | 105^{\S} |
| $R(= \Omega/2\pi)$ | 0.17 ± 0.04 | * | * |
| EW [eV] (Fe K α line) | 21 | 18 | 18 |
| (c) f | 0.21 ± 0.03 | 0.21^{\S} | $0.40^{+0.26}_{-0.15}$ |
| (d) N_{H}^1 | $7.9^{+1.4}_{-1.3}$ | 7.9^{\S} | $2.9^{+1.6}_{-1.0}$ |
| (d) N_{H}^2 | 0.75 ± 0.03 | 0.75^{\S} | $0.49^{+0.17}_{-0.33}$ |
| χ^2/dof | 926.9/812 | 201.1/182 | 192.7/181 |

NOTE. — Errors are 90% confidence level for a single parameter.

(a) Intrinsic luminosity in the 2–10 keV band corrected for both Galactic and intrinsic absorptions in units of $10^{43} \text{ ergs s}^{-1}$.

(b) Galactic absorption column density in units of 10^{22} cm^{-2} .

(c) Covering fraction.

(d) Intrinsic absorption column density in units of 10^{22} cm^{-2} .

\S Parameters fixed at these values.

* We assume the same reflection component as that determined in epoch 1.

spectra (either of the two epochs) in the 1–60 keV band and *Swift* spectrum in the 14–195 keV band simultaneously, in all following analysis. The flux normalization between the *Suzaku* (XIS-FIs) and BAT spectra are set free, to take into account the time variability. In analyzing the spectra of epoch 2, we always fix the reflection component to that determined from the epoch 1 data.

Table 2 summarizes the results using the same phenomenological model (cutoff power law) as adopted in section 3.3. For epoch 2, we consider two extreme cases as the cause of the spectral variability from epoch 1 that (1) only the continuum changed without change of the absorber and that (2) only the absorber changed with the same continuum except for its normalization. We obtain similarly good fits for the two cases, and thus both possibilities are plausible from the spectral analysis. In reality, however, it may be difficult to explain such a short time ($< 10^4$ sec) variability by the absorber alone. If the absorber makes Kepler motion at $\sim 1000 r_{\text{g}}$, a typical location of the broad line region in AGNs, it moves only $\sim r_{\text{g}}$ in 10^4 sec, by assuming the black hole mass of $10^{7.8} M_{\odot}$. Thus, unless the emitting region is extremely small (like $< \text{several } r_{\text{g}}$), it is unlikely that crossing blobs in the line of sight can cause the large variability as observed.

3.4. Spectral Analysis with Comptonization Model

In this subsection, we analyze the spectra of 4C 50.55 with a physically motivated model instead of the phenomenological “cutoff power law” model, which is a mathematical approximation of the X-ray spectra of AGNs. Such analysis of AGN spectra has been very limited so far, since it requires high quality broad band data. As we will discuss in section 3.5, the contribution from the jet components is very small in the X-ray band. Hence, we consider that the origin of the continuum emission is predominantly thermal Comptonization of soft (ultra-violet) photons off hot electrons in the corona located above the accretion disk. Accordingly, we adopt a

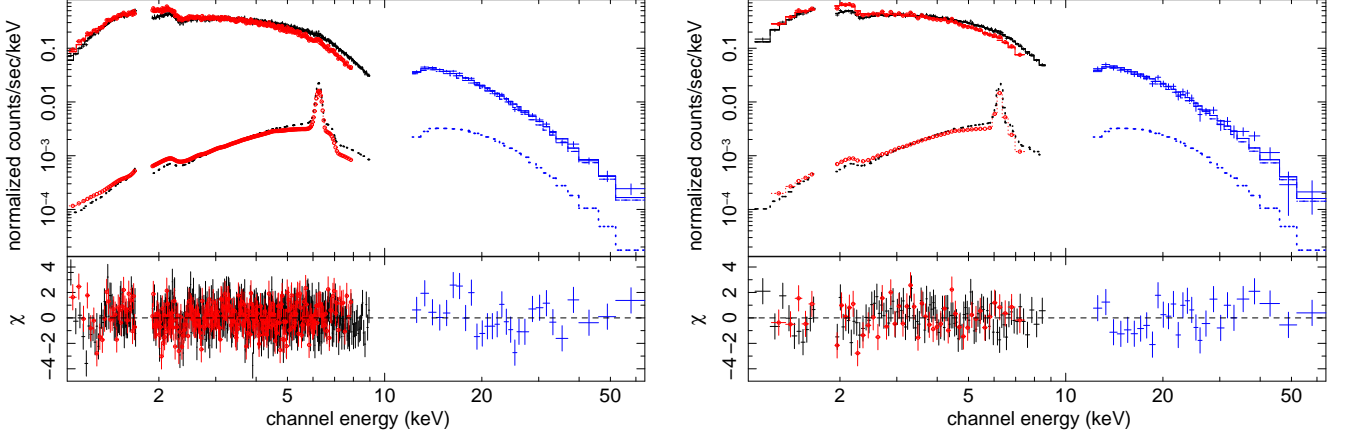


FIG. 4.— (a) (*left*) The folded spectra of 4C 50.55 in epoch 1 obtained with the XIS-FIs in the 1–9 keV band (black), the XIS-BI in the 1–8 keV band (red, open circle), and the PIN in the 12–60 keV band (blue). The solid curve represents the best-fit model (see Table 1). The dotted curve represents the reflection component. (b) (*right*) those in epoch 2.

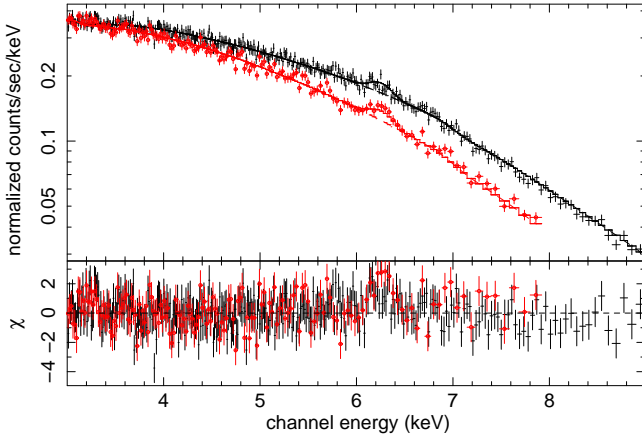


FIG. 5.— (*upper*) The spectra of 4C 50.55 obtained with the XIS-FIs (black) and XIS-BI (red, open circle) in epoch 1. The best-fit model (see Table 1) is plotted by the solid curve. The dashed curve indicates the model from which the iron-K emission line is excluded. (*lower*) The residuals of the fit in units of χ for the model without the iron-K line.

thermal Comptonization model, **thComp** (Zycki et al. 1999), for the primary continuum. It has two free parameters, the slope Γ and electron temperature kT_e . The electron scattering optical depth τ_e is related to T_e and Γ by the following formula (Sunyaev & Titarchuk 1980):

$$\tau_e = \sqrt{2.25 + \frac{3}{(T_e/511 \text{ keV})[(\Gamma + 0.5)^2 - 2.25]}} - 1.5(1)$$

For seed photons, we assume a multicolor disk component with the innermost temperature of 0.01 keV. This choice is not important to constrain the Comptonization parameters. As described in the previous subsection, the reflection component and fluorescence iron-K line are self-consistently included, which are blurred by the “diskline” profile with the same parameters as obtained above ($r_{\text{in}} = 720r_g$).

We perform simultaneous fit to the *Suzaku* (epoch 1 or 2) and *Swift*/BAT spectra using this model. The best-fit

TABLE 3
BEST-FIT PARAMETERS OF COMPTONIZATION MODEL TO THE COMBINED *Suzaku* AND *Swift* DATA

| Parameters | Epoch 1 & BAT | Epoch 2 & BAT |
|--|---------------------|---------------------|
| (a) $L_{2-10} \text{ keV}$ | 8.4 | 9.6 |
| (b) $N_{\text{H}}^{\text{gal}}$ | 1.0^{\S} | 1.0^{\S} |
| Γ | 1.78 ± 0.02 | 1.81 ± 0.01 |
| $kT_e \text{ [keV]}$ | 31^{+10}_{-6} | 46^{+37}_{-13} |
| (c) (τ_e) | $2.8^{+0.4}_{-0.5}$ | $2.1^{+0.5}_{-0.8}$ |
| $R(= \Omega/2\pi)$ | 0.16 ± 0.04 | * |
| $EW \text{ [eV]} \text{ (Fe } K\alpha \text{ line)}$ | 19 | 17 |
| (d) f | 0.27 ± 0.02 | 0.27^{\S} |
| (e) N_{H}^1 | $8.6^{+1.1}_{-1.0}$ | 8.6^{\S} |
| (e) N_{H}^2 | 0.80 ± 0.03 | 0.80^{\S} |
| χ^2/dof | 942.5/812 | 200.8/182 |

NOTE. — Errors are 90% confidence level for a single parameter.

(a) Intrinsic luminosity in the 2–10 keV band corrected for both Galactic and intrinsic absorptions in units of $10^{43} \text{ ergs s}^{-1}$.

(b) Galactic absorption column density in units of 10^{22} cm^{-2} .

(c) Electron-scattering optical depth calculated from the equation (1).

(d) Covering fraction.

(e) Intrinsic absorption column density in units of 10^{22} cm^{-2} .

\S Parameters fixed at these values.

* We assume the same reflection component as that determined in epoch 1.

parameters are summarized in Table 3. We obtain the electron temperature of $\approx 30 \text{ keV}$ with an optical depth of ≈ 3 . Again, the reflection component in epoch 2 are fixed at the same one determined from epoch 1. We find that the continuum parameters are consistent each other between epochs 1 and 2 within the statistical errors at the 90% confidence level. Figure 6 shows the results in the two epochs, in the form of unfolded spectra (i.e., those corrected for the effective area of the instruments) in units of $E I(E)$, where E is photon energy and $I(E)$ the energy flux.

3.5. Multi-Wavelengths Spectral Energy Distribution

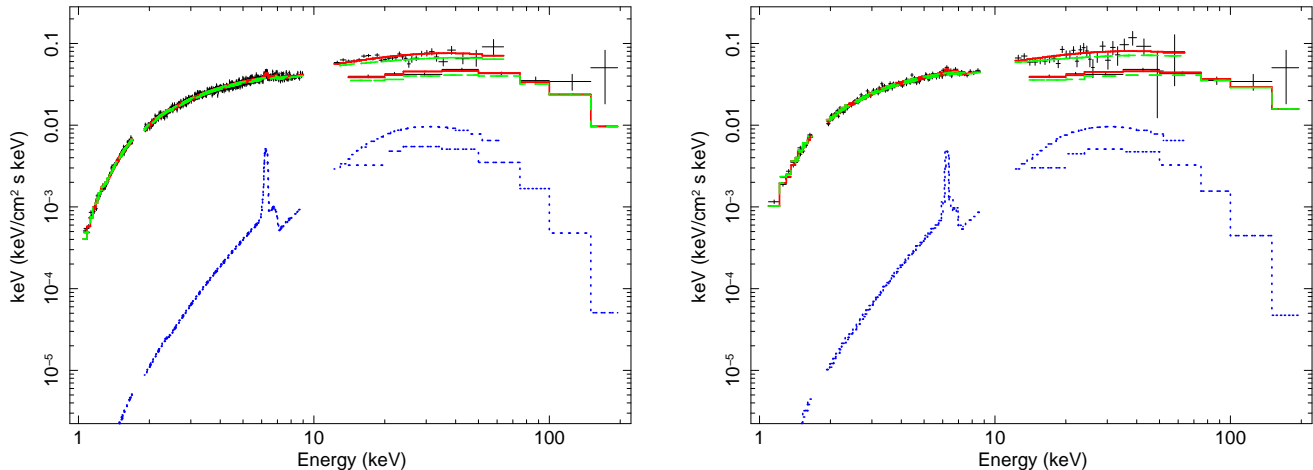


FIG. 6.— (a) (*left*) The unfolded spectra of 4C 50.55 determined from the *Suzaku* data in epoch 1 and from the *Swift*/BAT data, based on a thermal Comptonization model. The crosses (black) represent the data points, dashed curve (blue) the transmitted component, dashed curve (magenta) the reflection component, and solid curve (red) the total. The best-fit parameters are given in Table 3. (b) (*right*) those in epoch 2.

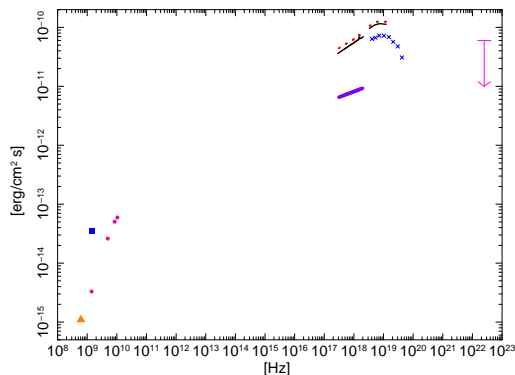


FIG. 7.— The SED of 4C 50.55. The solid (black) and dotted (red) curves represent the *Suzaku* spectra in epochs 1 and 2, respectively, while the thick (purple) one represents their difference spectrum between the two epochs. The spectrum of *Swift*/BAT is shown by the blue crosses. The pink arrow represents the upper limit on the γ -ray flux from the *Fermi* data (Abdo et al. 2009). The radio data are taken after Molina et al. (2007); the orange filled-triangle and reddish violet filled-circles represent the core flux obtained from the GMRT (Pandey et al. 2006) and the VLA, respectively. The blue filled-square represent the total flux including both core and lobes.

We summarize in Figure 7 the available multi-wavelengths fluxes of 4C 50.55 to discuss its spectral energy distribution (SED) from the radio to γ -ray bands. In the radio band, we utilize those obtained by the VLA and the Giant Metrewave Radio Telescope (GMRT) compiled by Molina et al. (2007). In the GeV γ -ray band, the upper limit derived from the one-year *Fermi* data (Abdo et al. 2009) is indicated by the arrow. We plot the results of cutoff power law fit to the *Suzaku* spectra in epochs 1 (black) and 2 (red) as well as the time-averaged *Swift*/BAT data, correcting for both Galactic and intrinsic absorptions. To examine the origin of the time variability, we analyze the difference spectrum of XIS-FIs between epochs 2 and 1. Fitting with a single power law with the same double absorption as given in Table 1, we find $\Gamma \approx 1.8$. This result is also plotted in the figure (green curve).

Assuming that the global intrinsic SED of the jet emis-

sion in 4C 50.55 is similar to that of jet dominated-sources (Kubo et al. 1998) with correction for an estimated beaming factor ($\delta \sim 1$ for 4C 50.55 and $\delta \sim 10$ for blazars), the predicted X-ray emission is a factor of $\sim 10^{1-4}$ less than the observed X-ray flux. We thus conclude that X-ray emission due to a jet via synchrotron emission or inverse Compton should be very small in the total X-ray emission of this source. Based on the *Suzaku* results, the ratio of the core luminosity at 5 GHz and that in the 2–10 keV band is estimated to be $\log R_X = -3.6$. Thus, while 4C 50.55 should be classified as a radio loud object (Terashima & Wilson 2003), its radio to X-ray power ratio is much lower compared with typical blazars and more powerful radio galaxies, like 3C 120 ($\log R_X = -2.1$) (Kataoka et al. 2007). This confirms the conclusion by Molina et al. (2007), who did not find any evidence for an additional power law component representing the jet emission in the *XMM-Newton* spectrum.

We note that the optical fluxes of 4C 50.55 are highly uncertain at present due to the extinction (both Galactic and intrinsic ones), which could largely affect the empirical estimate of the black hole mass. In fact, the extinction-corrected AGN continuum flux at 5100 Å adopted by Winter et al. (2010) falls far below an extrapolation from the X-ray spectra toward lower energies. As a more simple approach, assuming typical SEDs of AGNs (Elvis et al. 1994; Grupe et al. 2010), we roughly estimate the 5100 Å flux to be $(0.7 - 8) \times 10^{-10}$ erg $\text{cm}^{-2} \text{s}^{-1}$ from the BAT flux averaged for 22 months. Then, from the luminosity at 5100 Å, $(0.6 - 7) \times 10^{44}$ erg s^{-1} , and the width of the H_β line, 2320 km s^{-1} FWHM (Winter et al. 2010), we derive the black hole mass of 4C 50.55 to be $\sim 10^{7.8 \pm 0.3} M_\odot$, using the formula given by Vestergaard & Peterson (2006). This is about 10 times higher than the estimate ($10^{6.58 \pm 0.07} M_\odot$) by Winter et al. 2010. Nevertheless, the suggestion that the black hole in 4C 50.55 accretes with a high Eddington ratio still holds. With a typical bolometric correction factor ($L_{\text{bol}}/L_{2-10 \text{ keV}} = 30$), we estimate the fraction of Eddington luminosity of 4C 50.55 to be $L_{\text{bol}}/L_{\text{Edd}} \sim 0.4$.

4. SUMMARY AND DISCUSSION

We have obtained the first simultaneous, broad band X-ray spectra of 4C 50.55 over the 1–60 keV band with *Suzaku*. These provide one of the best quality high energy data so far obtained from BLRGs. From the SED, we conclude that there is little contribution from jets in the X-ray emission, which is thus dominated by Comptonization by hot corona. We find that the overall continuum is represented by a cutoff power law, or a thermal Comptonization model, with complex intrinsic absorptions. We show that at least two absorber with different covering fractions and column densities are necessary to model the spectrum. The photon index and cutoff energy of 4C 50.55 are within the distribution of previous observations of BLRGs (Grandi et al. 2006), although both are somewhat smaller ($\Gamma \approx 1.6$ and $E_{\text{cut}} \approx 100$ keV) compared with typical values found from Seyfert galaxies ($\Gamma \approx 1.9$ and $E_{\text{cut}} \sim 200$ keV, Dadina 2008). These findings on 4C 50.55 are fully consistent with the results by Molina et al. (2007) from the *XMM-Newton* and *INTEGRAL* data observed on earlier epochs. We estimate that the corona responsible for Comptonization is optically thick for scattering $\tau_e \approx 3$ and is relatively cool $T_e \approx 30$ keV. The optical depth is larger and the temperature is lower than those obtained from Seyfert galaxies with thermal Comptonization models (e.g., Lubinski et al. 2010), as expected from the comparison in Γ and E_{cut} .

From our observations, time variability of the X-ray flux on both long ($\gtrsim 10^6$ sec) and short ($\sim 10^4$ sec) time scales is detected. The averaged 2–10 keV flux was the highest in our *Suzaku* observation among those in the previous observations reported in Molina et al. (2007) by a factor of 1.3–2.5. The hard X-ray flux in the 17–100 keV band (1.8×10^{-10} erg cm $^{-2}$ s $^{-1}$) was also higher by 1.4 than the averaged flux over 22-months obtained with *Swift*/BAT (1.3×10^{-10} erg cm $^{-2}$ s $^{-1}$). The large long-term variability in the hard X-ray above 10 keV suggests that it is mainly produced by the intrinsic emission, not purely by the change of the absorber as discussed by Molina et al. (2007) in the frame work of a “patch torus” model (Elitzur & Shlosman 2006). While there remains a possibility that Compton thick absorber ($N_{\text{H}} > 10^{24}$ cm $^{-2}$) may completely cover a part of the emission region to cause the flux variability, it would produce signals of heavy obscuration such as a deep iron-K edge feature in the X-ray spectra, which are not seen in the data. Thus, at least variability of the continuum flux is required to explain these results, while that of the absorber can also contribute to the variability, in particular below 10 keV (Risaliti et al. see e.g., 2005 for NGC 1365).

We significantly detect an iron-K emission line and obtain a tight constraint on the reflection component, even though it is quite weak as reported by Molina et al. (2007). The reflection strength, $R \simeq 0.2$ is much smaller compared with Seyfert 1 galaxies, which typically have $R \sim 1$ (Dadina 2008). Even correcting for a variability effect that the direct continuum flux was higher in our observations by a factor of ≈ 1.4 than the 22-months average, the reflection is still small, $R \simeq 0.3$. The weak reflection is also consistent with the narrow iron-K emission line, which indicates that the reflection is mainly produced by relatively outer parts of the disk (hence with a small solid angle), unlike the results from typical Seyfert

1 galaxies (Dadina 2008). Our 4C 50.55 result confirms the trend reported by Sambruna et al. (2002) for radio loud AGNs.

The analysis of the iron-K line profile yields an (apparently) large innermost radius, $r_{\text{in}} \sim 700r_{\text{g}}$, by assuming an emissivity law of r^{-3} . Our diskline result suggests it unlikely that a “standard disk” extends down to close to the innermost stable circular orbit (ISCO) around the black hole, $< 6 r_{\text{g}}$. Instead, it is possible that the disk is there but its inner part is covered by an optically thick corona, as estimated by our Comptonization model fit, which would smear out relativistic iron-K broad lines. Note that the obtained r_{in} value does not directly mean that the disk is truncated at that radius, because (1) the estimated r_{in} critically depends on the emissivity profile and (2) there may be another line component from distant parts, such as the torus. If the scale height of the X-ray irradiating corona is sufficiently small, then one would expect a flatter slope for the emissivity law, even close to r^{-2} . In this extreme case, we were not able to obtain good constraints on r_{in} from our data. To examine the second possibility, we apply a two-components line model to the XIS 3–9 keV spectra, consisting of a narrow Gaussian at 6.4 keV and a broad diskline, which represents that from the torus and disk, respectively. We obtain a worse fit than the single diskline fit by $\Delta\chi^2 = 5$ even with a larger degrees of freedom, suggesting that the two components model is not a good description of the data. Nevertheless, when r_{in} of the disk line component is fixed at $10 r_{\text{g}}$ as found from 3C 120 (Kataoka et al. 2007), both lines are found to be significant with equivalent widths of 19 ± 6 eV and 24 ± 15 eV, respectively. Thus, we do not completely exclude the possibility for the presence of a moderately broadened iron-K line in the observed spectra of 4C 50.55.

The inferred geometry of the accretion disk in 4C 50.55 (i.e., truncated and/or inner parts covered by corona) may be common features of AGNs with powerful jets. Recent *Suzaku* studies indicate that radio galaxies also have relatively narrow iron-K emission lines e.g., $r_{\text{in}} > 20 r_{\text{g}}$ for 3C 390.3 (Sambruna et al. 2009) and $r_{\text{in}} > 44 r_{\text{g}}$ for 4C +74.26 (Larsson et al. 2008) from the single diskline fit, and $r_{\text{in}} = (9 \pm 1)r_{\text{g}}$ for 3C 120 from the multiple components fit (Kataoka et al. 2007). This result is in accordance with an expectation from theories that jets are more easily produced by radiatively inefficient accretion flow than by a standard disk.

Another key parameter to understand the accretion flow is the Eddington ratio, which is estimated to be $L_{\text{bol}}/L_{\text{Edd}} \sim 0.4$ for 4C 50.55 (section 3.5). Similarly, we also estimate that of 3C 120 to be $L_{\text{bol}}/L_{\text{Edd}} \sim 0.5$, using the 2–10 keV flux (Kataoka et al. 2007) and the black hole mass of $10^{7.7} M_{\odot}$ (Peterson et al. 2004). Thus, these two sources may belong to a very similar class of AGNs, except for the radio loudness to the X-ray flux ($\log R_{\text{X}} = -2.1$ for 3C 120 and $\log R_{\text{X}} = -3.6$ for 4C 50.55), which could be partially explained by the small inclination angle of 3C 120 ($i < 14^\circ$; see Kataoka et al. 2007) compared with 4C 50.55 ($i \sim 35^\circ$). The physical reason for the difference in their X-ray spectra that the reflection component and iron-K lines are stronger in 3C 120 ($R \sim 0.7$) is not clear at present.

4C 50.55 and 3C 120 are rare objects having

distinctively high fractions of Eddington luminosity compared with other typical BLRGs, for instance, $L_{\text{bol}}/L_{\text{Edd}} = 0.01\text{--}0.07$ for 3C 390.3 (Sambruna et al. 2009; Lewis & Eracleous 2006), ~ 0.04 for 4C +74.26 (Larsson et al. 2008), and $0.001\text{--}0.002$ for Arp 102B (Lewis & Eracleous 2006). By analogy to the Galactic black holes, these low Eddington ratio sources likely correspond to the low/hard state, where the accretion disk is accompanied by steady jets, while normal Seyfert galaxies may do to the high/soft state, where the disk extends close to the ISCO with quenched jet activity. The accretion flows in 4C 50.55 and 3C 120 could be explained as a high luminosity end of the low/hard state. Alternatively, they may be another state achieved with even higher mass accretion rates than in the high/soft state, where the disk structure is also similar to that found in the low/hard state (i.e., truncated disk). For this possibility, it is interesting to note the similarity to the high-Eddington ratio Galactic black hole GRS 1915+105, which exhibits a similarly narrow iron-K emission line over a Comptonization dominated continuum, imply-

ing that the inner disk is fully covered by a corona (Ueda et al. 2010); in GRS 1915+105, a compact jet is also detected in a steady state with a hard spectrum, so-called in Class χ (see e.g., Fender & Belloni 2004). In summary, the unified picture of accretion flows over a wide range of black hole mass is far from established. Further systematic studies of the accretion disk structure of radio loud AGNs at various accretion rates based on detailed X-ray spectroscopy and multi-wavelengths data are very important to reveal these fundamental problems.

We thank Gerry Skinner for providing the *Swift*/BAT light curve of 4C 50.55, and the *Suzaku* team for the calibration of the instruments. Part of this work was financially supported by Grants-in-Aid for Scientific Research 20540230 (YU) and 20740109 (YT), and by the grant-in-aid for the Global COE Program “The Next Generation of Physics, Spun from Universality and Emergence” from the Ministry of Education, Culture, Sports, Science and Technology (MEXT) of Japan.

REFERENCES

- Abdo, A. A., et al. 2009, *ApJS*, 183, 46
 Anders, E. & Grevesse, N. 1989, *Geochimica et Cosmochimica Acta*, 53, 197
 Bird, A. J. et al. 2004, *ApJ*, 607, 33
 Dadina, M. 2008, *A&A*, 485, 417
 Elitzur M., & Shlosman, I. 2006, *ApJ*, 648, 101
 Elvis, M., Wilkes, B. J., McDowell, J. C., Green, R. F., Bechtold, J., Willner, S. P., Oey, M. S., Polonski, E., & Cutri, R. 1994, *ApJS*, 95, 1
 Fabian, A. C., Rees, M. J., Stella, L., & White, N. E. 1989, *MNRAS*, 238, 729
 Fender, R. & Belloni, T. 2004, *ARA&A*, 42, 317
 Fender, R. P., Belloni, T. M., & Gallo, E. 2004, *MNRAS*, 355, 1105
 Fukazawa, Y., Mizuno, T., Takahashi, H., Enoto, T., Kokubun, M., Watanabe, S., & the HXD team 2008, *JX-ISAS-SUZAKU-MEMO-2008-01*
 Giovannini, G., Feretti, L., Gregorini, L., & Parma, P. 1988, *A&A*, 199, 73
 Grandi, P., Malaguti, G., & Fiocchi, M. 2006, *ApJ*, 642, 113
 Gruber, D. E., Matteson, J. L., Peterson, L. E., & Jung, G. V. 1999, *ApJ*, 520, 124
 Grupe, D., Komossa, S., Leighly, K. M., & Page K. L. 2010, *ApJS*, 187, 64
 Ishisaki, Y., et al. 2007, *PASJ*, 59, 113
 Kalberla, P. M. W., Burton, W. B., Hartmann, D., Arnal, E. M., Bajaja, E., Morras, R., Pöppel, W. G. L. 2005, *A&A*, 440, 775
 Kataoka, J., et al. 2007, *PASJ*, 59, 279
 Komatsu, E., et al. 2009, *ApJ*, 180, 330
 Kubo, H., Takahashi, T., Madejski, G., Tashiro, M., Makino, F., Inoue, S., & Takahara, F. 1998, *ApJ*, 504, 693
 Larsson, J., Fabian, A. C., Ballantyne, D. R., & Miniutti, G. 2008, *MNRAS*, 388, 1037
 Lewis, K. T., & Eracleous, M. 2006, *ApJ*, 642, 711
 Lubinski, P., Zdziarski, A. A., Walter, R., Paltani, S., Beckmann, V., Soldi, S., Ferrigno, C., & Courvoisier, T. J.-L. 2010, *arXiv:1005.0842*
 Maeda, Y., et al. 2008, *JX-ISAS-SUZAKU-MEMO-2008-06*
 Magdziarz, P. & Zdziarski, A. A. 1995, *MNRAS*, 273, 837
 Massetti, N., Palazzi, E., Bassani, L., Malizia, A., & Stephen, J. B. 2004, *A&A*, 426, 41
 Mitsuda, K., et al. 2007, *PASJ*, 59, S1
 Molina, M., et al. 2007, *MNRAS*, 382, 937
 Pandey, M., Manchanda, R. K., Rao, A. P., Durouchoux, P., & Ishwara-Chandra 2006, *A&A*, 446, 471
 Peterson, B. M., et al. 2004, *ApJ*, 613, 682
 Risaliti, G., Elvis, M., Fabbiano, G., Baldi, A., & Zezas, A. 2005, *ApJ*, 623, 93
 Sambruna, R. M., et al. 2009, *ApJ*, 700, 1473
 Sambruna, R. M., Eracleous, M., & Mushotzky, R. F. 2002, *New A Rev.*, 46, 215
 Sunyaev, R. A., & Titauchuk, L. G. 1980, *A&A*, 86, 121
 Tueller, J., et al. 2008, *ApJ*, 681, 113
 Terashima, Y., & Wilson, A. S. 2003, *ApJ*, 583, 145
 Ueda, Y., et al. 2010, *ApJ*, 713, 257
 Vestergaard, M., & Peterson, B. M. 2006, *ApJ*, 641, 689
 Winter, L. M., Lewis, K. T., Koss, M., Veilleux, S., Keeney, B., & Mushotzky, R. F. 2010, *ApJ*, 710, 503
 Zycik, P. T., Done, C., & Smith, D. A. 1999, *MNRAS*, 309, 561